nature nanotechnology

Article

Transport by circulating myeloid cells drives liposomal accumulation in inflamed synovium

Joke Deprez [1,2,3], Rein Verbeke [1,2], Sofie Meulewaeter[1,2], Ilke Aernout [1,2], Heleen Dewitte[1,2], Tine Decruy[3], Julie Coudenys[3], Julie Van Duyse[4,5], Gert Van Isterdael [4,5], Dan Peer [6,7,8,9], Roy van der Meel [10], Stefaan C. De Smedt [1,2], Peggy Jacques[3], Dirk Elewaut [2,3,11] ✉ & Ine Lentacker [1,2,11] ✉

The therapeutic potential of liposomes to deliver drugs into inflamed tissue is well documented. Liposomes are believed to largely transport drugs into inflamed joints by selective extravasation through endothelial gaps at the inflammatory sites, known as the enhanced permeation and retention effect. However, the potential of blood-circulating myeloid cells for the uptake and delivery of liposomes has been largely overlooked. Here we show that myeloid cells can transport liposomes to inflammatory sites in a collagen-induced arthritis model. It is shown that the selective depletion of the circulating myeloid cells reduces the accumulation of liposomes up to 50–60%, suggesting that myeloid-cell-mediated transport accounts for more than half of liposomal accumulation in inflamed regions. Although it is widely believed that PEGylation inhibits premature liposome clearance by the mononuclear phagocytic system, our data show that the long blood circulation times of PEGylated liposomes rather favours uptake by myeloid cells. This challenges the prevailing theory that synovial liposomal accumulation is primarily due to the enhanced permeation and retention effect and highlights the potential for other pathways of delivery in inflammatory diseases.

Liposomes have been studied as drug carriers for over half a century[1,2] to improve the stability, bioavailability, pharmacokinetics and safety of a wide variety of drugs with various physicochemical properties[1,2]. Incorporating polyethylene glycol (PEG)-conjugated lipids in liposomal formulations is considered to be the gold standard to reduce liposomal clearance by the mononuclear phagocytic system[3,4], consequently prolonging the circulation time of liposomes[2,3]. This improves the accumulation of PEGylated liposomes at inflammatory sites like the

[1]Laboratory of General Biochemistry and Physical Pharmacy, Ghent Research Group on Nanomedicine, Ghent University, Ghent, Belgium. [2]Cancer Research Institute Ghent (CRIG), Ghent, Belgium. [3]Unit Molecular Immunology and Inflammation, VIB Centre for Inflammation Research, Ghent University and Department of Rheumatology, Ghent University Hospital, Ghent, Belgium. [4]VIB Flow Core, VIB Center for Inflammation Research, Ghent, Belgium. [5]Department of Biomedical Molecular Biology, Ghent University, Ghent, Belgium. [6]Laboratory of Precision Nanomedicine, Shmunis School of Biomedicine and Cancer Research, George S. Wise Faculty of Life Sciences, Tel Aviv University, Tel Aviv, Israel. [7]Department of Materials Sciences and Engineering, Iby and Aladar Fleischman Faculty of Engineering, Tel Aviv University, Tel Aviv, Israel. [8]Center for Nanoscience and Nanotechnology, Tel Aviv University, Tel Aviv, Israel. [9]Cancer Biology Research Center, Tel Aviv University, Tel Aviv, Israel. [10]Laboratory of Chemical Biology, Department of Biomedical Engineering and Institute for Complex Molecular Systems, Eindhoven University of Technology, Eindhoven, The Netherlands. [11]These authors contributed equally: Dirk Elewaut, Ine Lentacker. ✉e-mail: Dirk.Elewaut@UGent.be; Ine.Lentacker@UGent.be

synovium[5–8], often explained by the enhanced permeation and retention (EPR) effect[1,3]. This originates from Matsumura and Maeda's observation in the 1980s that intravenously injected macromolecules can passively extravasate into diseased sites due to the presence of poorly aligned endothelial cells[9] and is still largely accepted as the predominant reason for liposomal accumulation in tumours and inflamed lesions[5,7,10].

In contrast, it remains largely unexplored how and to what extent liposomes interact with circulatory myeloid cells, which is especially important when inflammatory diseases are targeted[11–13]. In rheumatoid arthritis (RA), it is known that circulating myeloid cells, such as monocytes and neutrophils, infiltrate the inflamed tissue and play a key role in the inflammatory process[12–15]. Myeloid cell infiltration has been exploited by several groups to develop monocyte or neutrophil-targeted nanoparticles, including liposomes, as a strategy to treat inflammatory diseases[16–19]. However, in-depth studies that clarify to what extent the myeloid cell transport of non-targeted liposomes contributes to their accumulation into inflamed tissues are currently lacking[20].

This study reveals that the prolonged blood circulation of PEGylated liposomes results in sustained engulfment by blood-circulating myeloid cells, which drives their subsequent accumulation into arthritic joints. We quantified that myeloid-cell-mediated transport is responsible for over 50% of liposome delivery in arthritic joints.

Circulatory myeloid cells massively engulf PEGylated liposomes

To investigate the impact of PEGylation on the ability of liposomes to accumulate in inflamed joints, the chronic inflammatory collagen-induced arthritis (CIA) mouse model was used (Fig. 1a). Starting from day 21, the mice were examined three times a week and the inflammation rate was visually scored on a scale from 0 (no signs) to 4 (severe inflammation with deformations). On inflammation, sustained myelopoiesis results in a chemotaxis-driven transport of myeloid cells from the bone marrow to the inflammatory joints[12,13]. We validated CIA induction by analysing blood and ankle synovium from healthy and CIA DBA/1 mice with flow cytometry. Figure 1b provides an overview of cell surface markers used to quantify (1) circulating monocytes that convert into monocyte-derived infiltrating macrophages (MoMFs) in the synovium, (2) neutrophils, (3) dendritic cells, (4) B-cells and (5) CCR2+ myeloid cells. Supplementary Figs. 1 and 2 show the detailed gating strategy. A much higher monocyte, neutrophil and B-cell fraction was found in the blood of CIA mice compared with healthy mice (Fig. 1c). Moreover, we observed a clear invasion of different myeloid cell populations (MoMFs, neutrophils, CCR2+ cells and dendritic cells) in the inflamed synovia (Fig. 1d). The increase in myeloid cells was less prominent in the blood (Fig. 1c) and can be explained by the limited circulation time of myeloid cells in the blood before synovial accumulation, as well as the prolonged half-life of MoMFs and neutrophils in the synovium[12,21].

As Fig. 1e illustrates, non-PEGylated and PEGylated liposomes (5 mol% DSPE-PEG) liposomes were prepared with comparable size

(Fig. 1f) and zeta potential (Fig. 1g). It is known that liposome size may change on intravenous injection due to the adsorption of serum proteins[1,3,22], which can result in aggregation. Therefore, we measured the liposome size after dispersing in foetal bovine serum (Supplementary Fig. 3). Although the size of the non-PEGylated liposomes increased by about 100 nm, the size of the PEGylated liposomes did not change. This indeed confirms that PEGylation improves the colloidal stability of the liposomes in serum[23].

Liposomes containing the near-infrared dye DiR were prepared to evaluate liposomal biodistribution (Fig. 1h–l) up to 24 h after intravenous administration[24,25] in healthy (Fig. 1i,j) and CIA mice (Fig. 1k,l). The fluorescence intensity of the throat region (Fig. 1i–l, blue circles) was used to estimate the blood circulation time of the liposomes, given its high blood perfusion and the fact that it is an unpigmented and almost furless region. The fluorescence intensity of the throat shows that the non-PEGylated liposomes have a circulation time of less than 4 h, whereas the PEGylated liposomes circulate longer than 24 h (Supplementary Fig. 4 and Fig. 1i–l). Although the blood circulation times of liposomes were similar in control and CIA mice, liposomal accumulation was only detected in the inflamed ankles and paws of CIA mice (Fig. 1k–l). This accumulation was much more prominent for the PEGylated liposomes and correlated well with the CIA score of the limbs (Fig. 1m).

Passive liposome accumulation in inflamed regions has been predominantly attributed to the EPR effect. Early reports demonstrated that liposome uptake by synovial macrophages occurred[8,26]. This was later termed 'ELVIS', that is, extravasation through leaky vasculature and subsequent inflammatory cell-mediated sequestration, and proposed to be a direct result of the EPR effect[5]. Although ELVIS acknowledges liposome uptake by immune cells at inflammation sites, it overlooks that the majority of macrophages are derived from circulating monocytes, which massively infiltrate the inflamed synovium from the blood (Fig. 1d)[27,28]. Therefore, we aimed to investigate whether myeloid cells already take up liposomes in the blood before their chemotactic recruitment to inflammatory sites and as such contribute to liposome accumulation in the synovium. Therefore, we quantified liposome uptake in different immune cells in the blood and ankle synovium.

Flow cytometry analysis with an exploratory panel (Fig. 1b and Supplementary Figs. 1 and 2) suggests liposomal engulfment by myeloid cells in the blood and ankle synovium (Supplementary Fig. 5a,b). In the latter (Fig. 2a), significantly more myeloid cells engulfed PEGylated liposomes compared with non-PEGylated liposomes and this percentage further increased over time, correlating with the progressive accumulation of PEGylated liposomes in the inflamed synovia (Fig. 1m). As shown in Fig. 2b, this also resembled the liposomal uptake profiles in the blood, which implies that liposome uptake by myeloid cells already occurred to a large extent in circulation and suggests that circulatory myeloid cells engulf liposomes in the blood and transport them towards the synovium. Similar observations were also observed in the inflamed knee synovium (Supplementary Fig. 6)[29]. To confirm this hypothesis, we visualized the uptake experiment of PEGylated

Fig. 1 | Characterization of the CIA model, the two different liposomes used in this study and their respective biodistribution over 24 h. a, CIA is induced by immunizing the mice with a collagen cocktail including complete Freund's adjuvant, which is followed by a boost immunization at day 21. Starting from that time point, the inflammation of the paws is visually scored on a scale from 0 to 4. In this study, only mice with at least one ankle joint with score 3 were included. **b**, Overview of cell surface markers used in our exploratory study. **c,d**, Absolute number of immune cell fractions in the blood (**c**) and ankle synovium (**d**) of healthy (grey) (N = 4) and CIA DBA/1 mice (N = 6) (blue). Data are represented as mean ± standard deviation (s.d.). Two-sided multiple t-test analysis performed with correction for multiple tests (Sidak). Significance levels are indicated with asterisks: *, ** and *** represent the adjusted p values of p < 0.05, p < 0.01 and

p < 0.001, respectively. **e**, Schematic of PEGylated and non-PEGylated liposomes. **f,g**, Size distribution and polydispersity index (PDI) (**f**) and zeta potential (**g**) of DSPC:Chol (40:60 mol%) (N = 6) and DSPC:Chol:PEG (38:57:5 mol%) (N = 9) liposomes dispersed in HEPES buffer; data are represented as mean ± standard error of the mean (s.e.m.). **h**, Representative image of a control DBA/1 mouse, that is, no liposomes were injected. **i–l**, Representative images of the biodistribution of DiR liposomes in healthy and CIA DBA/1 mice at 4 h (**i** and **k**) and 24 h (**j** and **l**) after intravenous injection. The blue circle indicates the neck–throat area; the fluorescence signal in this region allowed to estimate the blood-residence time of the liposomes. **m**, Correlation between the DiR fluorescence signal in the inflamed ankles and the CIA score of the ankles (N = 2). Data are represented as mean ± s.e.m.

liposomes via the Amnis ImageStream imaging flow cytometer (Fig. 2c). CD45$^+$CD11b$^+$ cells from blood and ankle synovium (Supplementary Fig. 7 shows the gating strategy) were sorted and ImageStream was used to visualize the liposomal uptake in monocytes

and neutrophils (Supplementary Fig. 8 shows the gating strategy). The internalization wizard of ImageStream demonstrated liposomal engulfment in both cell types (Fig. 2d), thereby confirming our hypothesis. Importantly, both ImageStream images (Fig. 2c
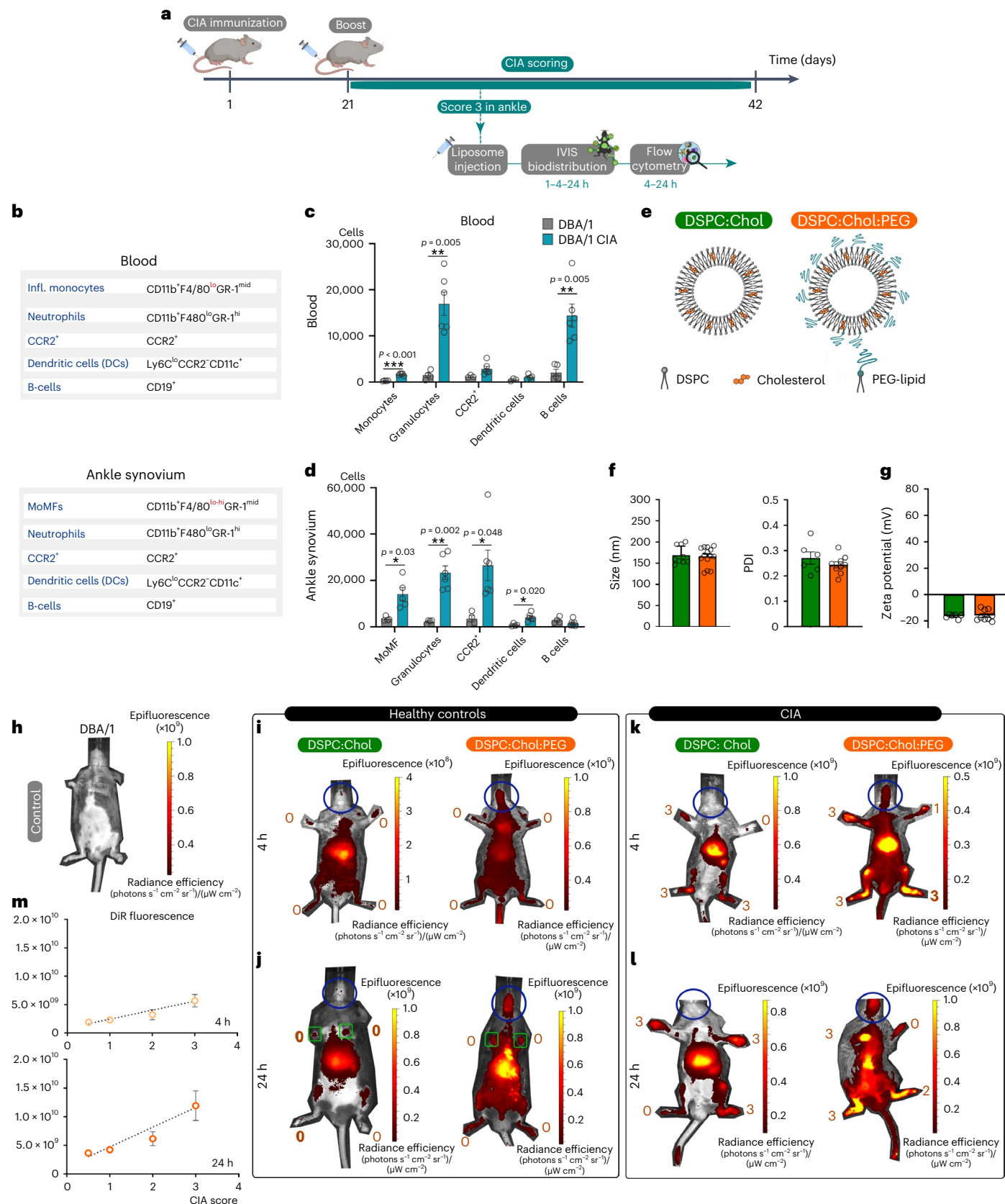
and Supplementary Figs. 9 and 10) and flow cytometry histograms (Fig. 2a,b) indicated a much higher liposome engulfment by monocytes than neutrophils.

To allow further phenotyping of the liposome-positive myeloid cells in blood and synovium, we repeated the exploratory uptake experiments (Fig. 2a–d) with a more advanced and extensive flow cytometry panel (Fig. 2e) and after the injection of PEGylated liposomes (Fig. 2f–i). This allowed the discrimination of neutrophils (CD45$^+$CD11b$^+$Ly6C$^+$Ly6G^{hi}), inflammatory monocytes (CD45$^+$CD11b$^+$Ly6C$^+$CCR2$^+$CX3CR1$^+$F4/80^{Lo}), monocyte-derived macrophages (CD45$^+$CD11b$^+$Ly6C$^+$CCR2$^+$CX3CR1$^+$F4/80^{hi}) and synovium-resident macrophages (F4/80^{hi}Ly6C$^-$CCR2$^-$CX3CR1$^-$) (refs. 30,31) (Supplementary Fig. 11 shows the gating strategy). The first observation was that liposome engulfment in the synovium was solely restricted to immune cells (CD45$^+$), particularly myeloid cells, whereas mesenchymal synovial fibroblasts (included in the CD45$^-$ population) did not take up liposomes (Supplementary Fig. 12a). Importantly, we could visualize the upregulation of macrophage marker F4/80 on synovium-infiltrating monocytes, confirming that the F4/80^{lo} monocytes in circulation are indeed the precursors of F4/80^{hi} MoMFs in the synovium (Fig. 2f). This also explains why these cells have comparable uptake profiles in blood and ankle synovium (Fig. 2g). Only 2.7% of the macrophages within the synovial fluid were identified as synovial resident macrophages (F4/80^{hi}Ly6C$^-$CCR2$^-$CX3CR1$^-$) (Supplementary Fig. 12b), and therefore, their contribution to liposome engulfment is negligible compared with the MoMFs (Supplementary Fig. 12b) in the CIA model. Figure 2g illustrates that all monocytes (blood and synovium) and MoMFs (synovium) engulfed the liposomes, whereas neutrophils do to a lesser extent (Fig. 2g), which corresponds well with the ImageStream data (Fig. 2c).

We also determined the relative contribution of monocytes and neutrophils to this liposomal transport by quantifying (1) the amount of monocytes, MoMF and neutrophils in liposome-positive cell fractions in the blood and ankle synovium (Fig. 2h) and (2) their liposomal uptake based on the mean fluorescence intensity (MFI) representing the number of liposomes engulfed (Fig. 2i). This illustrates that neutrophils are the largest fraction (78%) of liposome-positive CD45$^+$ cells in the blood, whereas monocytes account for less than 10%. This can be explained by the amount of circulating neutrophils versus monocytes in circulation (Fig. 1c). Interestingly, based on the MFI values, we observed that circulatory monocytes engulfed on average 5.6 times more liposomes compared with the neutrophils (Fig. 2i), which again corresponds to the ImageStream data (Fig. 2c). In contrast to blood, monocytes and MoMFs contributed to a much higher extent to liposome-positive myeloid cells in the synovium (Fig. 2h) as well as showed a higher liposome engulfment efficiency compared with neutrophils (Fig. 2i). Despite the higher fraction of neutrophils in circulation, these data (Fig. 2h,i), therefore, suggest that monocytes are mainly responsible for the cell-mediated liposome transport to the inflamed synovium due to their much higher phagocytic capacity. It is important to note that the maturation of monocytes into MoMFs in the synovium is accompanied

by a clear increase in MFI. This shows that the synovium-infiltrated monocytes continue to engulf liposomes at the synovium and suggests that ELVIS also partially contributes to the observed accumulation of liposomes in myeloid cells in the inflamed synovia.

## Adoptive cell transfer confirms myeloid cell transport

To further confirm that myeloid cells transport liposomes to the inflamed synovium, we performed an in situ adoptive cell transfer experiment using genetically altered (CD45.1, donor) and wild-type (CD45.2, recipient) C57BL/6 mice (Fig. 3a). It is known that a milder form of arthritis is induced in Th1-dominant CIA C57BL/6 mice[32] compared with Th2-dominant CIA DBA/1 mice; therefore, immune profiling and liposomal uptake experiments (Figs. 1 and 2a,b) were repeated to confirm that myeloid cell uptake was not impacted by the immunological background of the mice (Supplementary Figs. 13–17). Although a lower percentage of neutrophils was detected in the blood and synovium of the C57BL/6 mice, this did not impact the liposome uptake profile (Supplementary Figs. 15–17), but could explain why C57BL/6 mice are more resistant to the onset of inflammation[32,33] as neutrophils are indispensable for CIA initiation[34].

PEGylated liposomes were intravenously injected in CIA CD45.1 mice; 24 h later, peripheral blood leucocytes of CD45.1 mice were harvested and pooled before re-infusion in a CIA CD45.2 mouse (Fig. 3a). Importantly, the harvested leucocytes were centrifuged to remove free liposomes to guarantee that liposome delivery into the synovia was only cell mediated and no further uptake of free liposomes by CD45.1 cells was possible after transfusion. Figure 3b–d summarizes the outcome of two independent experiments. In the first experiment, 7.6×10^6 CD45.1 leucocytes were pooled for injection in one CD45.2 mouse, whereas in the second experiment, 12.6×10^6 CD45.1 leucocytes were pooled. Flow cytometry analysis confirmed the high viability (>99%) of the peripheral blood leucocytes before transfusion (Fig. 3b). Four hours after transfusion, the percentage of CD45.1 immune cells in blood and ankle synovium of the recipient CD45.2 mice was quantified with flow cytometry (Fig. 3c and Supplementary Figs. 18 and 19). A population of CD45.1 cells was found in the blood and in the inflamed synovia (Fig. 3c), which confirms myeloid cell infiltration into the inflamed tissue. The number of transfused cells found in the inflamed synovium was very low (<1% of the total number of synovial cells) in the first experiment, though expected given the high number of endogenous immune cells in the transfused mouse and the relatively low amount of CD45.1 leucocytes that were transfused. The experiment was, therefore, repeated with a higher number of transfused cells (12.5×10^6 CD45.1 leucocytes per CD45.2 mouse) to confirm the myeloid infiltration with a higher statistical significance (Fig. 3c). Figure 3d shows the flow cytometry histograms of the myeloid CD45.1 cells in the ankle synovium and reveals that the majority of MoMFs and CCR2$^+$ CD45.1 cells in the synovium contained liposomes, whereas only 27.2% of the infiltrated CD45.1 neutrophils contained liposomes.

Fig. 2 | Liposome engulfment by myeloid cells in CIA DBA/1 mice.
a,b, Liposome uptake in myeloid cells in the ankle synovium (**a**) and blood (**b**) as measured with the exploratory flow cytometry panel (Fig. 1b). The graphs show the percentage of liposome-positive cells for each myeloid cell type for non-PEGylated and PEGylated liposomes at 4 and 24 h after injection, respectively. Data are represented as mean ± s.e.m., sample size ($N = 4$) per condition, two-sided one-way analysis of variance analysis and adjusted p values with correction for multiple tests (Tukey's). The representative flow cytometry histograms are shown below each graph. **c**, Confirmation of liposome uptake (red; DiD liposome staining) by ImageStream flow cytometry. The images of monocytes and neutrophils (green; CD11b staining) in blood and ankle synovium, respectively, are shown. **d**, Degree of internalization can be defined using the internalization wizard of ImageStream software. The cell image that was masked is the CD45$^+$CD11b$^+$ population and liposome internalization (R2) was defined

using DiD as the probe for the liposomes. **e**, Overview of the extended flow cytometry panel in which additional myeloid cell markers were included to better phenotype the liposome-positive myeloid cell and macrophage population. **f**, Illustration of macrophage maturation (upregulation of F4/80) on synovium-infiltrated monocytes (CD45$^+$CD11b$^+$Ly6C$^+$CX3CR1$^+$CCR2$^+$). **g**, Confirmation of PEGylated liposome uptake in monocytes, MoMFs and neutrophils in the ankle synovium and blood, characterized using a more extensive panel in a repetition experiment. Data in **g**–**i** are represented as mean ± s.d.; sample size ($N = 3$) per condition. **h**, Respective contribution (%) of different myeloid cells within total liposome-positive CD45$^+$ cells in the blood and ankle synovium. **i**, MFI, representing the liposome uptake, in the myeloid cells in blood and ankle synovium. Two-sided unpaired t-test analysis was performed. Significance levels are indicated with asterisks: *, ** and *** represent the p values of $p < 0.05$, $p < 0.01$ and $p < 0.001$, respectively.
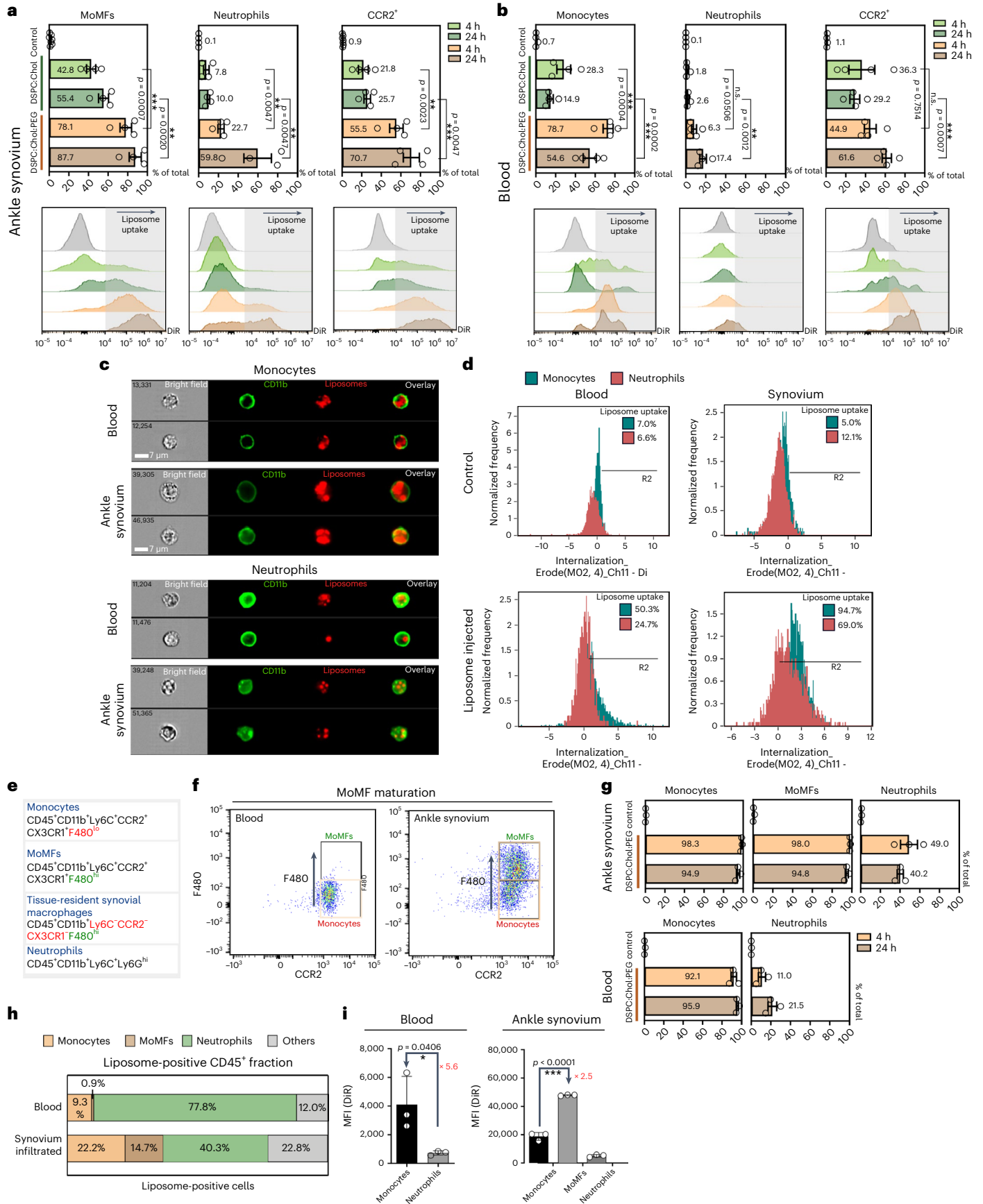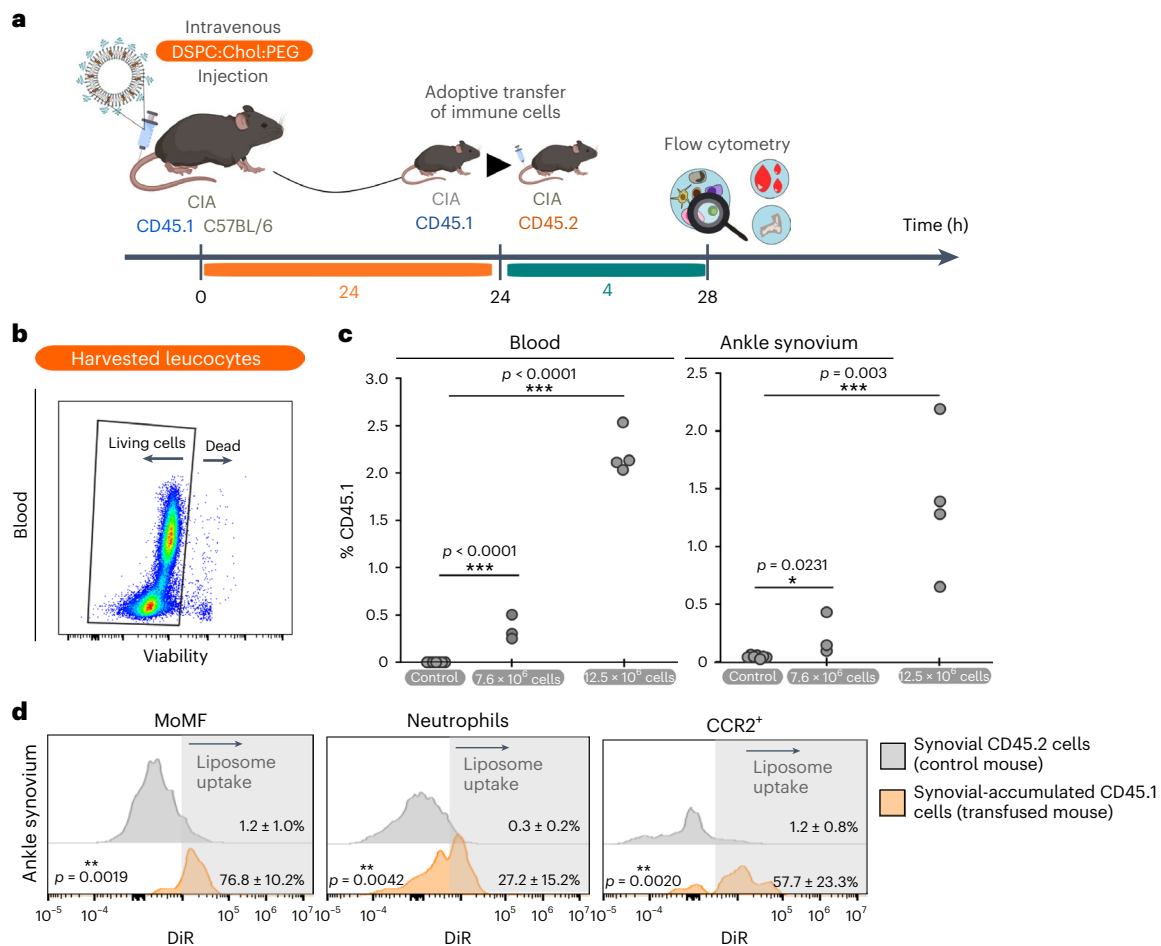
Fig. 3 | Adoptive cell transfer experiment in C57BL/6 CIA mice. a, CD45.1 C57BL/6 CIA mice were intravenously injected with DSPC:Chol:PEG liposomes. **b**, After 24 h of harvesting CD45.1 leucocytes from the blood and pooled, their viability was assessed. **c**, Different concentrations of pooled CD45.1 leucocytes (that is, 7.6×10^6 or 12.5×10^6 cells) were transfused in one CD45.2 C57BL/6 CIA mouse. Flow cytometry detection of transfused CD45.1 cells in the blood and inflamed synovium of the recipient mice was performed at 4 h after transfusion. Sample size, $N = 3$ and $N = 4$ mice for autologous transfusion with 7.6×10^6 and 12.6×10^6 transfused cells, respectively, and the corresponding controls; two-sided unpaired *t*-test analysis was performed. **d**, Flow cytometry histograms of liposome uptake within the transfused CD45.1 myeloid cells fraction (orange) retrieved in the ankle synovium of the recipient, compared with uptake in CD45.2 cells in the ankle synovium of control mice (grey). Sample size, $N = 7$ mice for control and $N = 7$ mice for autologous transfusion, pooled from two independently performed experiments with $N = 3$ and $N = 4$ mice, respectively; two-sided unpaired *t*-test analysis was performed. Significance levels in **c** and **d** are indicated with asterisks: *, ** and *** represent the *p* values of $p < 0.05$, $p < 0.01$ and $p < 0.001$, respectively.

The adoptive cell transfer experiment, thus, confirmed our earlier observations (Fig. 2) that liposome transport by myeloid cells from the circulation into inflamed synovia takes place and that monocytes as well as neutrophils are involved.

Selective cell depletion confirms myeloid cell transport

To quantify the contribution of myeloid-cell-mediated transport of PEGylated liposomes into inflamed synovia, we made use of myeloid-cell-depleted CIA mice by using anti-GR-1 and anti-CCR2 monoclonal antibodies (Fig. 4a). This experiment was performed twice in two independent experiments (Fig. 4c–g). Antibody treatment efficiently depleted circulating and synovium-infiltrating myeloid cells (Supplementary Fig. 21b) without affecting the CIA scores over the following 48 h (Fig. 4e). PEGylated liposomes were injected 24 h after the first antibody injection followed by the quantification of synovial liposome accumulation with IVIS imaging (Fig. 4b–g). We observed that liposome accumulation in inflamed front paws and ankles (score 3) of depleted mice was reduced by over 50% compared with control mice (Fig. 4c–g). Flow cytometry analysis confirmed that the uptake of PEGylated liposomes in CD45⁺ cells in the ankle synovium was

decreased by 60% (Fig. 4h). These results imply that the transport of PEGylated liposomes by myeloid cells is responsible for over 50% of liposome accumulation in inflamed synovia. Importantly, we observed that (1) on depletion of the myeloid fraction, liposome uptake remains restricted to the immune cell population (Supplementary Fig. 21a) and (2) part of the residual accumulation of the liposomes in the synovium of antibody-depleted mice may be explained by the remaining fraction of myeloid CD45⁺CD11b⁺CX3CR1⁺ cells that are triple negative for Ly6C, Ly6G and CCR2. This particular myeloid fraction also contributes to liposome accumulation in non-depleted conditions and transport does not seem to increase on depletion of the other myeloid fractions (Supplementary Fig. 21c).

Lipid nanoparticles containing mRNA show gene expression in inflamed joints

Next, we explored whether mRNA-containing PEGylated lipid nanoparticles (mRNA LNPs) made with the clinically relevant ionizable lipid MC3 were also taken up by myeloid cells in CIA C57BL/6 mice (Fig. 5 and Supplementary Fig. 21) as well as in CIA DBA/1 (Supplementary Fig. 22). The mRNA LNPs were prepared with firefly luciferase (*f*Luc) encoding N1-methylpseudouridine-modified mRNA and had a similar
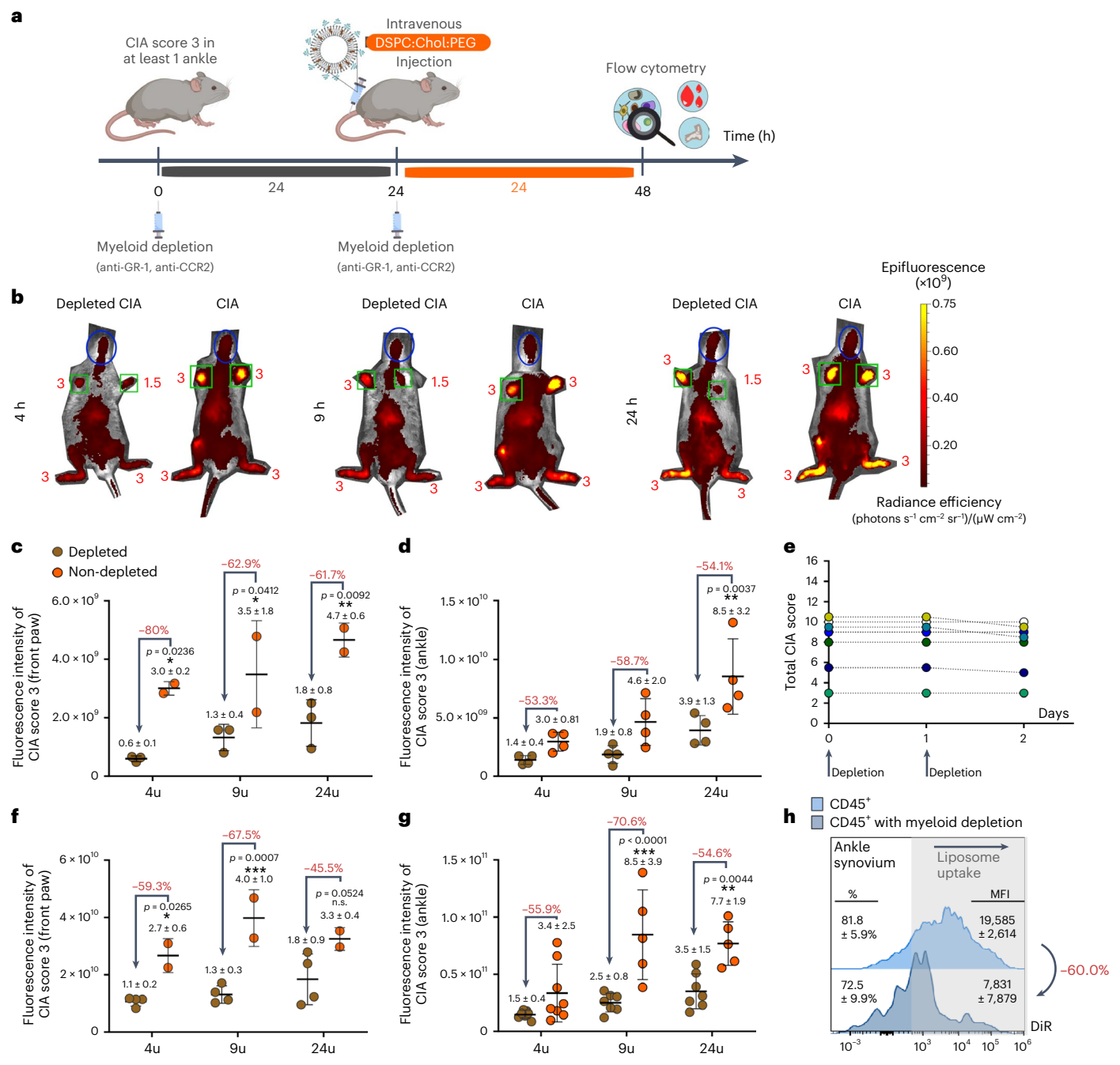
Fig. 4 | Liposome accumulation in myeloid-cell-depleted CIA mice.
a, Timeline of the myeloid cell depletion experiments. **b**, Representative in vivo biodistribution images of PEGylated liposomes in a myeloid-cell-depleted CIA DBA/1 mouse (left) and a control CIA DBA/1 mouse (right). Fluorescence intensity of all score-3 front paws (**c** and **f**) and ankles (**d** and **g**) in myeloid-cell-depleted CIA (brown dots) and non-depleted CIA control mice (orange dots). The experiment was performed twice, in two independent experiments with respective sample sizes of N = 3 mice (**c** and **d**) and N = 4 (**f** and **g**) for both CIA control and CIA depleted mice. Data are represented as mean ± s.d. and were analysed using a two-sided two-way analysis of variance analysis with correction for multiple tests (Sidak). Significance levels (**c**–**g**) are indicated with asterisks: *, ** and *** represent the adjusted p values of p < 0.05, p < 0.01 and p < 0.001, respectively. **e**, Effect of the intraperitoneal injection of depleting antibodies at day 0 and day 1 onto ankle inflammation. The total CIA score (sum of the visual score of four limbs) was monitored over 48 h and depicted in this graph. **h**, Uptake of liposomes in immune (CD45+) cells in the inflamed ankle synovia of myeloid-cell-depleted mice and control mice.

size and surface charge (Fig. 5b) as the PEGylated liposomes we studied. As the LNPs contained a 'diffusible' PEG lipid (PEG-DMG), we only performed experiments 4 h after intravenous injection due to their shorter circulation time.

After injection, mRNA LNPs accumulated in the joints (Fig. 5c and Supplementary Fig. 21), similar to the findings with PEGylated liposomes (Fig. 2). Furthermore, we observed a high fLuc expression

(Fig. 5c (right) and Supplementary Fig. 22a (right)) that corresponded well with the fluorescent signal (Fig. 5c (left) and Supplementary Fig. 22a (left)). The mRNA LNPs were also engulfed in myeloid cells, both in the blood and in the ankle synovium (Supplementary Fig. 22), and cellular uptake profiles in the ankle synovium (Fig. 5d and Supplementary Fig. 22b) were comparable with those of PEGylated liposomes. However, in blood, the percentage of myeloid cells that engulfed mRNA LNPs was
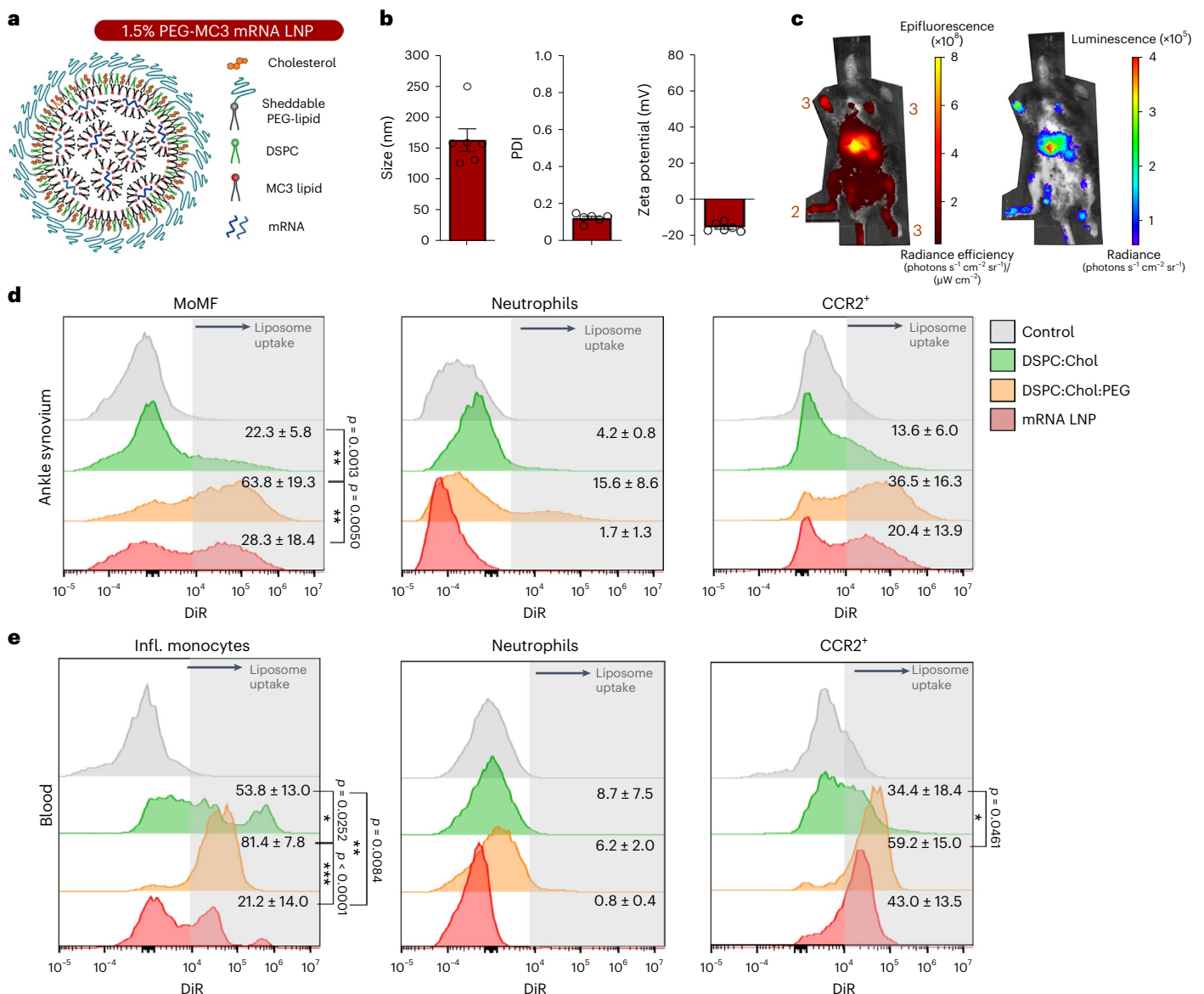
Fig. 5 | Physicochemical characterization and in vivo biodistribution of mRNA LNPs in CIA C57BL/6 mice. a, Schematic of the *f*Luc mRNA LNP. **b**, Size, PDI and zeta potential of mRNA LNPs. Data are represented as mean ± s.e.m. Sample size (*N* = 6). **c**, In vivo biodistribution (left) and luciferase expression (right) 4 h after intravenous injection. **d**,**e**, Representative flow cytometry histograms for liposome uptake in the most relevant myeloid cells in ankle synovium (**d**) and blood (**e**). Data are represented as mean ± s.d. Sample size (*N* = 3) per condition and two-sided two-way analysis of variance analysis with correction for multiple tests (Tukey). Significance levels are indicated with asterisks: *, ** and *** represent the adjusted *p* values of *p* < 0.05, *p* < 0.01 and *p* < 0.001, respectively.

notably lower compared with PEGylated liposomes (Fig. 5e). This could be expected as 4 h after injection, most of PEG-DMG was already dissociated from the LNPs[35–37]. It was estimated that the PEG-DMG half-life in LNPs was close to one hour only, which results in a much shorter circulation time of the 'diffusible' PEG-DMG-composed LNPs compared with PEGylated liposomes[37].

Within our study, we observed that inflammatory myeloid cells (that is, monocytes and neutrophils) engulfed PEGylated liposomes in circulation after the administration of PEGylated liposomes in a clinically relevant dose, similar to, for example, the FDA/EMA-approved Doxil/Caelyx. Moreover, the presence of chemotactic markers CCR2 and CX3CR1 on the surface of liposome-positive synovial macrophages confirmed their monocyte-derived myeloid origin[13,38–40]. With an autologous cell transfusion experiment, we showed that cytokine-driven myeloid-cell-mediated transport contributes to liposome accumulation in inflamed joints and this accounts for over 50% of liposome

accumulation in the inflamed joints based on the outcome after myeloid cell depletion. Although several studies have shown that ligand-modified nanoparticles actively engage in cellular transport by Ly6C-positive cells, macrophages, monocytes and neutrophils[17–19,41,42], our data suggest that cellular transport is also an important mechanism at play for unmodified nanoparticles. This study illustrates that monocytes—the circulating precursors of the majority of synovial macrophages in CIA—are especially efficient in liposome transport and this was more pronounced for long-circulating PEGylated liposomes. Our work, therefore, indicates that nanocarrier PEGylation does not completely abrogate immune cell uptake but, on the contrary, favours a sustained uptake in myeloid cells due to their long circulation time. In contrast, the much shorter circulation time (<4 h) of non-PEGylated liposomes limits the time frame for uptake by circulating myeloid cells and impedes their transport into the synovium. This observation is important given the fact that PEGylation is considered the gold

standard to avoid uptake by highly phagocytic immune cells of the mononuclear phagocytic system, such as macrophages and dendritic cells[3]. Although PEGylation has shown to slow down opsonization and immune recognition, the interaction of PEGylated liposomes with myeloid cells remains, however, less understood[5,43]. It was recently observed that neutrophils favour the uptake of C3 and C5 opsonized nanoparticles[44]; further in-depth exploration of protein corona formation kinetics on PEGylated liposomes could probably provide hints on how this might relate to uptake by myeloid cells[45–47]. It could also explain why monocytes seem to phagocytose more PEGylated liposomes compared with neutrophils, whereas both myeloid cell types are known to be highly phagocytic[48]. An alternative explanation can be found in the shorter circulation and survival time of neutrophils, which restricts the timeframe for phagocytosis.

We showed that MC3-based mRNA lipid nanoparticles are also taken up and transported to the inflamed synovium by circulating myeloid cells, inducing local mRNA expression. Therefore, our data correspond well to observations that the targeting of siRNA LNPs to myeloid cells could be improved by optimizing the LNP formulation[49,50]. Such optimized LNPs containing siRNA ameliorated inflammatory symptoms in rodents and non-human primates and provided the first indication that LNPs might be promising for anti-inflammatory treatments. Also, several recent reports showed that myeloid cells take up intramuscularly administered mRNA LNP COVID-19 vaccines and consequently release proinflammatory cytokines[51,52]. Importantly, it is worth highlighting that the presence of a PEG lipid on the nanocarrier seemed indispensable in inducing long-term uptake in circulating myeloid cells as we observed a drop in LNP uptake in circulating myeloid cells at 4 h post-intravenous injection that probably relates to the diffusible PEG[37].

Although we explored myeloid-cell-mediated transport in an RA model, it is known that the recruitment of myeloid cells plays a key role in many other diseases, including COVID-19 (refs. 53–57) and cancer[58–60]. Recent studies have identified inflammatory monocytes as important contributors to COVID-19-induced inflammatory responses and the subsequent cytokine storm[53,54,56,61]. Therefore, our findings support the idea proposed in another work to explore the use of PEGylated liposomes for delivering corticosteroids to macrophages in inflamed lungs[61]. Also, the passive accumulation of PEGylated liposomes in tumours has been extensively documented[10,62–64]. Following our findings, further research is warranted to investigate the contribution of myeloid-cell-mediated transport in this process.

Conclusions

In conclusion, we observed that myeloid-cell-mediated transport contributes to the accumulation of PEGylated liposomes at inflammatory sites, which has previously been primarily attributed to the EPR effect. Our findings suggest that exploiting the interactions between nanomaterials and immune cells may reveal attractive opportunities for the nanomedicine-based treatment of inflammatory diseases.

Online content

Any methods, additional references, Nature Portfolio reporting summaries, source data, extended data, supplementary information, acknowledgements, peer review information; details of author contributions and competing interests; and statements of data and code availability are available at https://doi.org/10.1038/s41565-023-01444-w.

References

1. Sercombe, L. et al. Advances and challenges of liposome assisted drug delivery. *Front. Pharmacol.* **6**, 286 (2015).
2. Giulimondi, F. et al. Interplay of protein corona and immune cells controls blood residency of liposomes. *Nat. Commun.* **10**, 3686 (2019).
3. Suk, J. S., Xu, Q., Kim, N., Hanes, J. & Ensign, L. M. PEGylation as a strategy for improving nanoparticle-based drug and gene delivery. *Adv. Drug Deliv. Rev.* **99**, 28–51 (2016).
4. Lundqvist, M. et al. Nanoparticle size and surface properties determine the protein corona with possible implications for biological impacts. *Proc. Natl Acad. Sci. USA* **105**, 14265–14270 (2008).
5. Ren, H. et al. Role of liposome size, surface charge, and PEGylation on rheumatoid arthritis targeting therapy. *ACS Appl. Mater. Interfaces* **11**, 20304–20315 (2019).
6. Yang, M., Feng, X., Ding, J., Chang, F. & Chen, X. Nanotherapeutics relieve rheumatoid arthritis. *J. Control. Release* **252**, 108–124 (2017).
7. Gawne, P. J. et al. PET imaging of liposomal glucocorticoids using 89 Zr-oxine: theranostic applications in inflammatory arthritis. *Theranostics* **10**, 3867–3879 (2020).
8. Metselaar, J. M. et al. Liposomal targeting of glucocorticoids to synovial lining cells strongly increases therapeutic benefit in collagen type II arthritis. *Ann. Rheum. Dis.* **63**, 348–353 (2004).
9. Matsumura, Y. & Maeda, H. A new concept for macromolecular therapeutics in cancer chemotherapy: mechanism of tumoritropic accumulation of proteins and the antitumor agent Smancs. *Cancer Res.* **46**, 6387–6392 (1986).
10. Danhier, F. To exploit the tumor microenvironment: since the EPR effect fails in the clinic, what is the future of nanomedicine? *J. Control. Release* **244**, 108–121 (2016).
11. Davignon, J. L. et al. Targeting monocytes/macrophages in the treatment of rheumatoid arthritis. *Rheumatology* **52**, 590–598 (2013).
12. Kaplan, M. J. Role of neutrophils in systemic autoimmune diseases. *Arthritis Res. Ther.* **15**, 219 (2013).
13. Izar, M. C. O. et al. Monocyte subtypes and the CCR2 chemokine. *Clin. Sci. (Lond.)* **131**, 1215–1224 (2017).
14. McInnes, I. B. & Schett, G. Pathogenetic insights from the treatment of rheumatoid arthritis. *Lancet* **389**, 2328–2337 (2017).
15. Dammes, N. et al. Conformation-sensitive targeting of lipid nanoparticles for RNA therapeutics. *Nat. Nanotechnol.* **16**, 1030–1038 (2021).
16. Sofias, A. M., Andreassen, T. & Hak, S. Nanoparticle ligand-decoration procedures affect in vivo interactions with immune cells. *Mol. Pharm.* **15**, 5754–5761 (2018).
17. Chu, D., Gao, J. & Wang, Z. Neutrophil-mediated delivery of therapeutic nanoparticles across blood vessel barrier for treatment of inflammation and infection. *ACS Nano* **9**, 11800–11811 (2015).
18. Karathanasis, E. et al. Selective targeting of nanocarriers to neutrophils and monocytes. *Ann. Biomed. Eng.* **37**, 1984–1992 (2009).
19. Veiga, N. et al. Leukocyte-specific siRNA delivery revealing IRF8 as a potential anti-inflammatory target. *J. Control. Release* **313**, 33–41 (2019).
20. Vargason, A. M., Anselmo, A. C. & Mitragotri, S. The evolution of commercial drug delivery technologies. *Nat. Biomed. Eng.* **5**, 951–967 (2021).
21. El Kebir, D. E. & Filep, J. G. Modulation of neutrophil apoptosis and the resolution of inflammation through β2 integrins. *Front. Immunol.* **4**, 60 (2013).
22. Braeckmans, K. et al. Sizing nanomatter in biological fluids by fluorescence single particle tracking. *Nano Lett.* **10**, 4435–4442 (2010).
23. Chen, D., Ganesh, S., Wang, W. & Amiji, M. Plasma protein adsorption and biological identity of systemically administered nanoparticles. *Nanomedicine* **12**, 2113–2135 (2017).
24. De Chermont, Q. L. M. et al. Nanoprobes with near-infrared persistent luminescence for in vivo imaging. *Proc. Natl Acad. Sci. USA* **104**, 9266–9271 (2007).
25. Smith, W. J. et al. Lipophilic indocarbocyanine conjugates for efficient incorporation of enzymes, antibodies and small molecules into biological membranes. *Biomaterials* **161**, 57 (2018).

26. Hofkens, W., Storm, G., Van Den Berg, W. B. & Van Lent, P. L. Liposomal targeting of glucocorticoids to the inflamed synovium inhibits cartilage matrix destruction during murine antigen-induced arthritis. *Int. J. Pharm*. **416**, 486–492 (2011).

27. Kratofil, R. M., Kubes, P. & Deniset, J. F. Monocyte conversion during inflammation and injury. *Arterioscler. Thromb. Vasc. Biol*. **37**, 35–42 (2017).

28. Gschwandtner, M., Derler, R. & Midwood, K. S. More than just attractive: how CCL2 influences myeloid cell behavior beyond chemotaxis. *Front. Immunol*. **10**, 2759 (2019).

29. Seeuws, S. et al. A multiparameter approach to monitor disease activity in collagen-induced arthritis. *Arthritis Res. Ther*. **12**, R160 (2010).

30. Tu, J. et al. Ontogeny of synovial macrophages and the roles of synovial macrophages from different origins in arthritis. *Front. Immunol*. **10**, 1146 (2019).

31. Hoeffel, G. et al. Adult Langerhans cells derive predominantly from embryonic fetal liver monocytes with a minor contribution of yolk sac–derived macrophages. *J. Exp. Med*. **209**, 1167–1181 (2012).

32. Inglis, J. J. et al. Collagen-induced arthritis in C57BL/6 mice is associated with a robust and sustained T-cell response to type II collagen. *Arthritis Res. Ther*. **9**, R113 (2007).

33. Asquith, D. L., Miller, A. M., McInnes, I. B. & Liew, F. Y. Animal models of rheumatoid arthritis. *Eur. J. Immunol*. **39**, 2040–2044 (2009).

34. Wipke, B. T. & Allen, P. M. Essential role of neutrophils in the initiation and progression of a murine model of rheumatoid arthritis. *J. Immunol*. **167**, 1601–1608 (2001).

35. Akinc, A. et al. The Onpattro story and the clinical translation of nanomedicines containing nucleic acid-based drugs. *Nat. Nanotechnol*. **14**, 1084–1087 (2019).

36. Kulkarni, J. A., Witzigmann, D., Chen, S., Cullis, P. R. & Van Der Meel, R. Lipid nanoparticle technology for clinical translation of siRNA therapeutics. *Acc. Chem. Res*. **52**, 2435–2444 (2019).

37. Zhu, X. et al. Surface de-PEGylation controls nanoparticle-mediated siRNA delivery in vitro and in vivo. *Theranostics* **7**, 1990–2002 (2017).

38. Cambré, I. et al. Mechanical strain determines the site-specific localization of inflammation and tissue damage in arthritis. *Nat. Commun*. **9**, 4613 (2018).

39. Meghraoui-Kheddar, A., Barthelemy, S., Boissonnas, A. & Combadière, C. Revising CX3CR1 expression on murine classical and non-classical monocytes. *Front. Immunol*. **11**, 1117 (2020).

40. Kinne, R. W. Macrophages in rheumatoid arthritis. *Arthritis Res. Ther*. **2**, 189 (2000).

41. Veiga, N. et al. Cell specific delivery of modified mRNA expressing therapeutic proteins to leukocytes. *Nat. Commun*. **9**, 4493 (2018).

42. Wyatt Shields, C. et al. Cellular backpacks for macrophage immunotherapy. *Sci. Adv*. **6**, eaaz6579 (2020).

43. Kumar, R. A., Li, Y., Dang, Q. & Yang, F. Monocytes in rheumatoid arthritis: circulating precursors of macrophages and osteoclasts and, their heterogeneity and plasticity role in RA pathogenesis. *Int. Immunopharmacol*. **65**, 348–359 (2018).

44. Kim, J. & Sahay, G. Nanomedicine hitchhikes on neutrophils to the inflamed lung. *Nat. Nanotechnol*. **17**, 1–2 (2021).

45. Palchetti, S. et al. The protein corona of circulating PEGylated liposomes. *Biochim. Biophys. Acta Biomembr*. **1858**, 189–196 (2016).

46. Schöttler, S. et al. Protein adsorption is required for stealth effect of poly(ethylene glycol)- and poly(phosphoester)-coated nanocarriers. *Nat. Nanotechnol*. **11**, 372–377 (2016).

47. Francia, V., Schiffelers, R. M., Cullis, P. R. & Witzigmann, D. The biomolecular corona of lipid nanoparticles for gene therapy. *Bioconjugate Chem*. **31**, 2046–2059 (2020).

48. Dale, D. C., Boxer, L., & Liles, W. C. The phagocytes: neutrophils and monocytes. *Blood* **112**, 935–945 (2008).

49. Leuschner, F. et al. Therapeutic siRNA silencing in inflammatory monocytes in mice. *Nat. Biotechnol*. **29**, 1005–1010 (2011).

50. Novobrantseva, T. I. et al. Systemic RNAi-mediated gene silencing in nonhuman primate and rodent myeloid cells. *Mol. Ther. Nucleic Acids* **1**, e4 (2012).

51. Li, C. et al. Mechanisms of innate and adaptive immunity to the Pfizer-BioNTech BNT162b2 vaccine. *Nat. Immunol*. **23**, 543–555 (2022).

52. Lenart, K. et al. A third dose of the unmodified COVID-19 mRNA vaccine CVnCoV enhances quality and quantity of immune responses. *Mol. Ther. Methods Clin. Dev*. **27**, 309–323 (2022).

53. Jafarzadeh, A., Chauhan, P., Saha, B., Jafarzadeh, S. & Nemati, M. Contribution of monocytes and macrophages to the local tissue inflammation and cytokine storm in COVID-19: lessons from SARS and MERS, and potential therapeutic interventions. *Life Sci*. **257**, 118102 (2020).

54. Martinez, F. O., Combes, T. W., Orsenigo, F. & Gordon, S. Monocyte activation in systemic Covid-19 infection: assay and rationale. *eBioMedicine* **59**, 102964 (2020).

55. Zhang, D. et al. COVID-19 infection induces readily detectable morphologic and inflammation-related phenotypic changes in peripheral blood monocytes. *J. Leukoc. Biol*. **109**, 13–22 (2020).

56. Pence, B. D. Severe COVID-19 and aging: are monocytes the key? *GeroScience* **42**, 1051–1061 (2020).

57. Ragab, D., Salah Eldin, H., Taeimah, M., Khattab, R. & Salem, R. The COVID-19 cytokine storm; what we know so far. *Front. Immunol*. **11**, 1446 (2020).

58. Yoshimura, T. The production of monocyte chemoattractant protein-1 (MCP-1)/CCL2 in tumor microenvironments. *Cytokine* **98**, 71–78 (2017).

59. Parihar, A., Eubank, T. D. & Doseff, A. I. Monocytes and macrophages regulate immunity through dynamic networks of survival and cell death. *J. Innate Immun*. **2**, 204–215 (2010).

60. Yang, J., Zhang, L., Yu, C., Yang, X. F. & Wang, H. Monocyte and macrophage differentiation: circulation inflammatory monocyte as biomarker for inflammatory diseases. *Biomark. Res*. **2**, 1 (2014).

61. Lammers, T. et al. Dexamethasone nanomedicines for COVID-19. *Nat. Nanotechnol*. **15**, 622–624 (2020).

62. Benchimol, M. J., Bourne, D., Moghimi, S. M. & Simberg, D. Pharmacokinetic analysis reveals limitations and opportunities for nanomedicine targeting of endothelial and extravascular compartments of tumors. *J. Drug Target*. **27**, 690–698 (2019).

63. Fang, J., Nakamura, H. & Maeda, H. The EPR effect: unique features of tumor blood vessels for drug delivery, factors involved, and limitations and augmentation of the effect. *Adv. Drug Deliv. Rev*. **63**, 136–151 (2011).

64. Brocato, T. A. et al. Understanding the connection between nanoparticle uptake and cancer treatment efficacy using mathematical modeling. *Sci. Rep*. **8**, 7538 (2018).

Methods

Liposomes

The liposomes were produced using 1,2-distearoyl-sn-glycero-3-phosphocholine (DSPC; Corden Pharma), cholesterol (Avanti Polar Lipids) and 1,2-distearoyl-sn-glycero-3-phosphoethanolamine-N-(biotinyl(polyethyleneglycol)-2000) (DSPE-PEG$_{2000}$; Avanti Polar Lipids) in a 40:60:0 and 38:57:5 molar ratio using the lipid-film hydration technique reported elsewhere[65,66]. HEPES buffer (20 mM, pH 7.4) was used for the rehydration of the film, leading to a final lipid concentration of 12.5 mM lipids and subsequently downsized using a tip sonicator (Branson Digital Sonifier 450). For fluorescently labelled liposomes, a fluorescent lipid dye (either DiR/DiI) (Molecular Probes, Thermo Fisher Scientific) was added to the lipid solution before making the lipid film; the molar ratio (mol. dye$_{DiR/DiI}$:mol. total lipid) equalled 1.20:98.80, whereas (mol. dye$_{DiD}$:mol. total lipid) for ImageStream analysis equalled 0.25:99.75.

mRNA

Nucleoside-modified (N1mΨ) mRNA encoding ƒLuc and N1mΨ mRNA encoding ovalbumin were produced as described elsewhere[67].

Production of mRNA LNPs

LNPs containing mRNA were prepared as previously described[68,69]. Briefly, lipid components (DLin-MC3-DMA, DSPC, cholesterol and PEG-DMG) were dissolved in ethanol at appropriate molar ratios (50.0:10.0:38.5:1.5) to a final concentration of 10 mM total lipid. Then, mRNA was dissolved in 25 mM sodium acetate buffer at pH 4.0 to obtain a ratio of 0.056 mg nucleic acid per µmol lipid (corresponding to an amine-to-phosphate ratio of 3). The organic and aqueous solutions were mixed through a T-junction mixer[70,71] at a flow ratio of 1:3 (v:v) and a total flow rate of 28 ml min^{-1}. The resting suspension was dialysed against a 1,000-fold volume of phosphate-buffered saline at pH 7.4 overnight and concentrated using Vivaspin centrifugal concentrators. The lipid concentrations were determined by measuring the cholesterol content of the LNPs (Cholesterol E Assay, Wako Chemicals). The Quant-iT RiboGreen RNA Assay was used to determine the mRNA encapsulation and concentration in LNPs according to the manufacturer's protocols (Thermo Fisher).

Size and zeta potential of liposomes and LNPs

The intensity-based z-averaged size of the liposomes, the number-based size of the LNPs and zeta potential of all the formulations dispersed in the HEPES buffer (20 mM, pH 7.4) were characterized via dynamic light scattering using a Malvern ZetaSizer Nano ZS (Malvern Instruments).

Liposome aggregation assay in serum

A dispersion of fluorescently DiI liposomes with a total concentration of 12.5 mM lipids was 1:5,000 diluted in full foetal bovine serum (Biowest) or HEPES buffer (20 mM, pH 7.4) (control) and kept at 37 °C. The aggregation of liposomes up to 4 h was studied by fluorescent nanoparticle tracking using a NanoSight LM10 instrument (Malvern Instruments)[22].

Mice

Male DBA/1 and C57BL/6 mice were purchased from Janvier. Transgenic CD45.1 C57BL/6 mice were bred in situ (LA1400410). All the animals were housed in a specific-pathogen-free facility following institutional guidelines. Animal experiments were conducted according to the regulations of Belgian law and approved by the Local Ethical Committee on Animal Experiments (Ghent University, ECD 18/16). Mice were kept in controlled conditions (12 h/12 h light–dark cycle; temperature, 21–24 °C; relative humidity, 40–70%) and had access to food and water ad libitum.

CIA model

The CIA mouse model is frequently employed to investigate nanomedicines for RA[72] given its high similarities with human RA due to the activation of both innate and adaptive immune system[33,72]. The latter is lacking in other inflammatory models like the collagen-antibody-induced arthritis model and the lipopolysaccharide-induced acute inflammation model[73]. The CIA model was induced in male DBA/1 and C57BL/6 mice via intradermal injection at the base of the tail consisting of 200 µg of chicken type-II collagen (CII) (Morwell Diagnostics) dissolved in 0.1 M acetic acid, emulsified in incomplete Freund's adjuvant with 150 µg (DBA/1) and 200 µg (C57BL/6) Mycobacterium tuberculosis H37RA (Difco). After 21 days, a booster intradermal injection was given consisting of 200 µg CII in incomplete Freund's adjuvant (DBA/1) or 200 µg CII emulsified in incomplete Freund's adjuvant with 250 µg Mycobacterium tuberculosis H37RA (C57BL/6). DBA1 and C57BL/6 mice were monitored up to 42 and 60 days post-immunization, respectively. From day 21, the mice were monitored thrice per week for clinical symptoms of CIA. The severity of inflammation was visually scored based on erythema and swelling, and graded as follows: 0, normal; 0.5, erythema and oedema in only one digit; 1, erythema and mild oedema of the footpad, or ankle or two to five digits; 2, erythema and moderate oedema of two joints (footpad and ankle; two to five digits); 3, erythema and severe oedema of the entire paw; 4, reduced swelling and deformation leading to an incapacitated limb.

Intravenous injection of liposomes in mice

Healthy and CIA mice were anaesthetized via the inhalation of 3.5% isoflurane (IsoFlo, AST Farma) diluted with oxygen (0.5 l min^{-1}). The mice were injected via a catheter (polyethylene tubing, Intramedic PE10, BD) placed in the tail vein. The catheter was filled with a sterile 0.9% NaCl solution to ensure correct insertion in the tail vein. Once correctly placed, 200 µl of liposome dispersion was slowly injected. Before injection, the liposome dispersions were diluted in sterile isotonic HEPES buffer containing 5% glucose to reach a final lipid concentration of 1.2 mM. For the LNP formulation, the LNPs were diluted in sterile isotonic HEPES buffer containing 5% glucose to reach a dose of 10 µg mRNA per mouse based on the RiboGreen RNA Assay (see above). It is important to note that all liposome dispersions had the same (total) lipid concentration (that is, 6.25 mg ml^{-1}) and consisted of a comparable size; it should also be noted that for all dispersions, the same volume was intravenously injected.

Biodistribution of liposomes

The changes in biodistribution of the intravenously injected DiR liposomes were verified via repeated measurements using the IVIS Lumina II (PerkinElmer) in the far-red region at 745 nm. To enhance the detection of liposomes in the major organs, the body and limbs of the mice were depilated to maximize the fluorescence to be picked up by the IVIS device. Fluorescence images were acquired (acquisition time, 1 s) following excitation at 745 (±30) nm using an indocyanine green (ICG) emission filter. To estimate the blood circulation time of the liposomes, either free circulating or engulfed by circulating immune cells, the fluorescence from liposomes in the well-perfused, furless and non-pigmented 'throat–neck' area was measured, to estimate the residual fluorescence in the blood circulation. The quantification of the fluorescence images was done using the Living Image software (PerkinElmer version 4.7.4).

Luciferase expression

In vivo luciferase expression was measured for 10 min following the intraperitoneal injection of 100 µl of a luciferin solution (33 mg ml^{-1}, Vivoglo Luciferin, Promega) using the luminescence mode on IVIS Lumina II (PerkinElmer) with 5 min acquisition time.

Flow cytometry

The mice were euthanized via cervical dislocation and whole blood was subsequently collected in EDTA tubes (Sarstedt). Subsequently, the liver, lungs, spleen and hind legs were harvested. After single-cell suspensions were obtained, a red blood cell lysis step was performed.

The synovium was removed from the hind legs post bone marrow flushing and subsequently digested enzymatically using 1.00 mg ml⁻¹ dispase and 0.75 mg ml⁻¹ collagenase. In healthy mice, the harvested synovia of three mice were pooled from the ankles of the mice ($N = 12$ mice in total pooled into $N = 4$ samples). This was not required in the case of CIA mice as a much higher number of infiltrated immune cells were present in the synovium ($N = 4$ mice). Finally, the cells were stained with antibodies for flow cytometry. The panel consisted of Zombie Yellow viability dye, Fc block, CD45 brilliant violet 425, CD19 brilliant violet 425, CD11b-PerCP-Cy5.5, CD11c-PerCP-Cy5.5, F4/80-APC, Ly6G-APC, Ly6C-APC, GR-1-FITC and CCR2-FITC (BioLegend). The samples were analysed using CytoFLEX (Beckman Coulter). For the more extensive myeloid flow panel, the viability dye VioBlue (dump), CD45-VioGreen, CD11b-FITC, F480-PE-Vio615, Ly6C-PerCP-Vio770, CD19-VioBlue (dump), CD3e-VioBlue (dump), CD68-PE-Vio770 and CCR2-APC (purchased from Miltenyi) and NK1.1-BV421 (dump), Ly6G-BV607 and CX3CR1-PE (purchased from BioLegend) were combined. The samples were analysed using the MACSQuant flow cytometer (Miltenyi). All the flow cytometry data were analysed using FlowJo software (BD Biosciences version 10.8.1).

Myeloid cell sorting and ImageStream flow cytometry

Living myeloid cells (CD45⁺CD11b⁺) of both liposome-injected and control mice were sorted from blood and ankle synovium using BD FACS Aria III (BD Biosciences). Supplementary Fig. 9 shows the sorting strategy. Next to the liposome colour (DiD), Fc block (BioLegend), the panel consisted of eFluor 780 viability dye (Thermo Fisher), CD45-VioGreen (Miltenyi), CD11b-FITC (Miltenyi), Ly6G-BV607 (BioLegend) and Ly6C-PerCP-Vio770 (Miltenyi). After sorting, the selected cells were measured on ImageStream^X Mark kII (Amnis), where the liposome uptakes in the monocyte and neutrophil fraction were separately evaluated. Supplementary Fig. 10 shows the gating strategy. To verify the uptake of liposomes in myeloid cells, the internalization wizard provided by the IDEAS analysis software (Amnis version 6.3.23.0) was used. For this, the CD11b staining was used for the cell image, whereas liposome dye DiD was used as the internalization probe. An erode mask was then set on the cells of 4 pixels (Supplementary Fig. 13).

In situ autologous transfusion

DSPC:Chol:PEG liposomes were injected in the tail vein of CD45.1 CIA C57BL/6 mice with a CIA score of at least 3 in one of the limbs (front or hind leg). After 24 h, peripheral blood was collected in an EDTA tube and directly processed by a red blood cell lysis step. Subsequently, the blood was centrifuged (10 min, $500 \times g$) to remove the 'free liposomes' (that is, liposomes that are not taken up by cells) and subsequently pooled per three mice. The pooled sample was centrifuged and resuspended in maximum 200 μl isotonic NaCl solution and intravenously injected in a CD45.2 CIA C57BL/6 mouse with at least a CIA score of 3 in two hind legs (ankles). Each transfusion contained 7.4×10^6 CD45.1 leucocytes, with about 9.4% liposome-positive leucocytes, leading to an infusion of about 690,000 liposome-positive CD45.1 leucocytes into each CIA CD45.2 mouse. Four hours post-injection, the peripheral blood and ankle synovium were collected and processed as described before. Flow cytometry was performed using the original flow panel but the CD19 brilliant violet 425 marker was interchanged by the CD45.1 brilliant violet 425 marker (BioLegend) to identify the transfused immune cell population. The samples were analysed using CytoFLEX (Beckman Coulter). The experiments were repeated with a higher number of transfused CD45.1 leucocytes (12.5×10^6 cells). For this, the samples were analysed using the MACSQuant flow cytometer (Miltenyi).

Liposome accumulation after myeloid cell depletion in CIA mice

Twenty-four hours before liposome injection, the myeloid cells of mice with a CIA score of at least 3 in one of the hind legs were depleted;

therefore, an antibody cocktail of anti-CCR2-mAb (12.5 μg per mouse) (BioLegend) and anti-GR-1-mAb (150.0 μg per mouse) (BioLegend) was intraperitoneally injected. DSPC:Chol:PEG liposomes were then injected in the tail vain of the depleted CIA DBA/1 mice, together with a second intraperitoneal injection of the antibody cocktail to guarantee the complete depletion of myeloid cells over 48 h. At the same time, the control group (that is, regular non-depleted CIA DBA/1 mice with a similar CIA score) were injected with the exact same DSPC:Chol:PEG liposomes. Twenty-four hours after liposome injection, the peripheral blood and ankle synovium were harvested and processed as described above in both depleted and non-depleted mice.

Statistical analysis

The applicable statistical test is mentioned under each graph. Statistical analysis is performed using GraphPad Prism 6 (GraphPad). Significance levels are indicated with asterisks: *, ** and *** represent the adjusted p values of $p < 0.05$, $p < 0.01$ and $p < 0.001$, respectively.

Reporting summary

Further information on research design is available in the Nature Portfolio Reporting Summary linked to this article.

Data availability

The data supporting the findings of this study are available within the Article and its Supplementary Information. Other relevant data are available for research purposes from the corresponding authors upon request. Source data are provided with this paper.

References

65. Avnir, Y. et al. Amphipathic weak acid glucocorticoid prodrugs remote-loaded into sterically stabilized nanoliposomes evaluated in arthritic rats and in a Beagle dog: a novel approach to treating autoimmune arthritis. *Arthritis Rheum.* **58**, 119–129 (2008).
66. Avnir, Y. et al. Fabrication principles and their contribution to the superior in vivo therapeutic efficacy of nano-liposomes remote loaded with glucocorticoids. *PLoS ONE* **6**, e25721 (2011).
67. Verbeke, R. et al. Broadening the message: a nanovaccine co-loaded with messenger RNA and α-GalCer induces antitumor immunity through conventional and natural killer T cells. *ACS Nano* **13**, 1655–1669 (2019).
68. Kulkarni, J. A. et al. Fusion-dependent formation of lipid nanoparticles containing macromolecular payloads. *Nanoscale* **11**, 9023–9031 (2019).
69. Kulkarni, J. A. et al. On the formation and morphology of lipid nanoparticles containing ionizable cationic lipids and siRNA. *ACS Nano* **12**, 4787–4795 (2018).
70. Hirota, S., De Ilarduya, C. T., Barron, L. G. & Szoka, F. C. Simple mixing device to reproducibly prepare cationic lipid-DNA complexes (lipoplexes). *Biotechniques* **27**, 286–290 (1999).
71. Kulkarni, J. A. et al. Rapid synthesis of lipid nanoparticles containing hydrophobic inorganic nanoparticles. *Nanoscale* **9**, 13600–13609 (2017).
72. Kannan, K., Ortmann, R. A. & Kimpel, D. Animal models of rheumatoid arthritis and their relevance to human disease. *Pathophysiology* **12**, 167–181 (2005).
73. Seemann, S., Zohles, F. & Lupp, A. Comprehensive comparison of three different animal models for systemic inflammation. *J. Biomed. Sci.* **24**, 60 (2017).

Acknowledgements

Author contributions

I.L., D.E. and S.C.D.S. designed the project. J.D. was responsible for the protocols and project management. J.D., S.M. and I.A. carried out the liposome fabrication. J.D., R.V., S.M., I.A., H.D., T.D., J.C. and I.L. carried out the mice experiments. T.D. and J.C. were responsible for scoring, caretaking and harvesting the mice. J.D., R.V., S.M. and I.A. performed the IVIS imaging of the mice. J.V.D. and G.V.I. conducted the ImageStream experiments via the VIB Flow Core. J.D., I.L. and D.E. conceptualized the autologous transfusion experiment. J.D., D.P., S.M. and I.L. contributed to the conceptualization of the depletion experiment. J.D. analysed the data. R.v.d.M. helped with the fabrication and guidance of the mRNA LNPs. J.D., R.V. and I.L. wrote the manuscript with input from S.C.D.S, D.E., P.J. and R.v.d.M. All the authors contributed to the discussions and the final work.

Competing interests

The authors declare no competing interests.

Additional information

Supplementary information The online version contains supplementary material available at https://doi.org/10.1038/s41565-023-01444-w.

Correspondence and requests for materials should be addressed to Dirk Elewaut or Ine Lentacker.

Peer review information *Nature Nanotechnology* thanks Katharina Maisel and the other, anonymous, reviewer(s) for their contribution to the peer review of this work.

Reprints and permissions information is available at www.nature.com/reprints.

Corresponding author(s): Deprez Joke

Last updated by author(s): Apr 13, 2023

Reporting Summary

Nature Portfolio wishes to improve the reproducibility of the work that we publish. This form provides structure for consistency and transparency in reporting. For further information on Nature Portfolio policies, see our Editorial Policies and the Editorial Policy Checklist.

Statistics

For all statistical analyses, confirm that the following items are present in the figure legend, table legend, main text, or Methods section.

n/a	Confirmed	
☐	☒	The exact sample size (*n*) for each experimental group/condition, given as a discrete number and unit of measurement
☐	☒	A statement on whether measurements were taken from distinct samples or whether the same sample was measured repeatedly
☐	☒	The statistical test(s) used AND whether they are one- or two-sided *Only common tests should be described solely by name; describe more complex techniques in the Methods section.*
☒	☐	A description of all covariates tested
☐	☒	A description of any assumptions or corrections, such as tests of normality and adjustment for multiple comparisons
☐	☒	A full description of the statistical parameters including central tendency (e.g. means) or other basic estimates (e.g. regression coefficient) AND variation (e.g. standard deviation) or associated estimates of uncertainty (e.g. confidence intervals)
☐	☒	For null hypothesis testing, the test statistic (e.g. *F*, *t*, *r*) with confidence intervals, effect sizes, degrees of freedom and *P* value noted *Give P values as exact values whenever suitable.*
☒	☐	For Bayesian analysis, information on the choice of priors and Markov chain Monte Carlo settings
☒	☐	For hierarchical and complex designs, identification of the appropriate level for tests and full reporting of outcomes
☒	☐	Estimates of effect sizes (e.g. Cohen's *d*, Pearson's *r*), indicating how they were calculated

Our web collection on statistics for biologists contains articles on many of the points above.

Software and code

Policy information about availability of computer code

Data collection	No code was used for data collection.
Data analysis	Graphpad Prism 8.0, FlowJo Software, Ideas Software, Living Image Software, IDEAS Software

For manuscripts utilizing custom algorithms or software that are central to the research but not yet described in published literature, software must be made available to editors and reviewers. We strongly encourage code deposition in a community repository (e.g. GitHub). See the Nature Portfolio guidelines for submitting code & software for further information.

Data

Policy information about availability of data

All manuscripts must include a data availability statement. This statement should provide the following information, where applicable:
- Accession codes, unique identifiers, or web links for publicly available datasets
- A description of any restrictions on data availability
- For clinical datasets or third party data, please ensure that the statement adheres to our policy

Source data are provided with this paper. All data supporting the findings of this study are available within the paper and its Supplementary Information.

Field-specific reporting

Please select the one below that is the best fit for your research. If you are not sure, read the appropriate sections before making your selection.

☒ Life sciences ☐ Behavioural & social sciences ☐ Ecological, evolutionary & environmental sciences

For a reference copy of the document with all sections, see nature.com/documents/nr-reporting-summary-flat.pdf

Life sciences study design

All studies must disclose on these points even when the disclosure is negative.

Sample size	For animal studies, we made sure to have a minimal sample size of N=7, executed in two independently executed experiments, from which the mean ± SD/SEM was calculated and allowing to determine statistical significance.
Data exclusions	No mice were excluded from the experiments.
Replication	All in vivo experiments were carried out with a minimal sample size of N=7, executed in two independently executed experiments, that could either be replication in the same or in another mouse strain: i.e. DBA/1, C57BL/6 and C57BL/6 transgenic CD45.1.
Randomization	Mice with a CIA score of 3 in at least one of the ankles were randomized into similar groups to enable direct comparison between different liposome types and experiments.
Blinding	Blinding was not performed since all collected data were reported as measured. All samples were treated in the same manner for each experiment.

Reporting for specific materials, systems and methods

We require information from authors about some types of materials, experimental systems and methods used in many studies. Here, indicate whether each material, system or method listed is relevant to your study. If you are not sure if a list item applies to your research, read the appropriate section before selecting a response.

Materials & experimental systems

n/a	Involved in the study
☐	☒ Antibodies
☒	☐ Eukaryotic cell lines
☒	☐ Palaeontology and archaeology
☐	☒ Animals and other organisms
☒	☐ Human research participants
☒	☐ Clinical data
☒	☐ Dual use research of concern

Methods

n/a	Involved in the study
☒	☐ ChIP-seq
☐	☒ Flow cytometry
☒	☐ MRI-based neuroimaging

Antibodies

Antibodies used	Flow cytometry liposome uptake experiments:
	CD45-VioGreen, anti-mouse, Miltenyi, 130-110-803, Clone REA737
	CD11b-VioBright FITC, anti-mouse, Miltenyi, 130-113-805, Clone REA592
	CD19-Vioblue, anti-mouse, Miltenyi, 130-112-041, Clone REA749
	F4/80-PE-Vio615, anti-mouse, Miltenyi, 130-123-913, Clone REA126
	Ly6C-PerCP-Vio700, anti-mouse, Miltenyi, 130-111-920, Clone REA796
	CD192 (CCR2)-APC, anti-mouse, Miltenyi, 130-119-658, Clone REA538
	CD3ε-Vioblue, anti-mouse, Miltenyi, 130-118-849, Clone 17A2
	CD68-PE-Vio770, anti-mouse, Miltenyi, 130-118-849, Clone REA835
	NK1.1-BV421, anti-mouse, Biolegend, 108731, Clone PK136
	Ly6G-BV605, anti-mouse, Biolegend, 127639, Clone 1A8
	CX3CL1-PE, anti-mouse, Biolegend, 149005, Clone SA011F11
	CCR2-FITC, anti-mouse, Biolegend, 150607, Clone SA203G11
	GR-1-FITC, anti-mouse, Biolegend, 108405, Clone RB6-8C5
	F4/80-FITC, anti-mouse, Biolegend, 123107, Clone BM8
	F4/80-APC, anti-mouse, ThermoFisher, 17-4801-82, Clone BM8
	Ly6C-APC, anti-mouse, Biolegend, 128015, Clone HK1.4
	Ly6G-APC, anti-mouse, Biolegend, 127613, Clone 1A8
	CD11c-PerCP-Cy5.5, anti-mouse, Biolegend, 117327, Clone N418
	CD11b-PerCP-Cy5.5, anti-mouse, Biolegend, 101227, Clone M1/70
	CD19-BV421, anti-mouse, Biolegend, 115537, Clone 6D5

CD45-BV421, anti-mouse, Biolegend, 103133, Clone 30-F11

Depletion antibodies:
CCR2, anti-mouse, Biolegend, 160102, Clone QA18A56
GR-1, anti-mouse, Biolegend, 108401, Clone RB6-8C5

FACS sorting and subsequent Imagestream analysis:
CD45-VioGreen, anti-mouse, Miltenyi, 130-110-803, Clone REA737
CD11b-VioBright FITC, anti-mouse, Miltenyi, 130-113-805, Clone REA592
Ly6C-PerCP-Vio700, anti-mouse, Miltenyi, 130-111-920, Clone REA796
Ly6G-BV605, anti-mouse, Biolegend, 127639, Clone 1A8
Viability dye-eFluor780, Thermo Fisher, 65-0865-14

Validation

All antibodies used for flow cytometry were validated for flow cytometry (Manufacturer's website) and titrated by us prior to use.
The depletion antibodies were verified in a trial experiment to validate their use (Supplementary Figure 15B)

Animals and other organisms

Policy information about studies involving animals; ARRIVE guidelines recommended for reporting animal research

Laboratory animals

mice, DBA/1, male, 8-10 weeks at CIA immunisation
mice, C57BL/6, male, 8-10 weeks at CIA immunisation
mice, C57BL/6 CD45.1 transgenic, male and female, 8-10 weeks at CIA immunisation

Wild animals

This study did not involve wild animals.

Field-collected samples

The study did not involve samples collected from the field.

Ethics oversight

The experiments were approved by the local Ethical Committee on Animal Experiments (Ghent University, ECD 18/16).

Note that full information on the approval of the study protocol must also be provided in the manuscript.

Flow Cytometry

Plots

Confirm that:

☒ The axis labels state the marker and fluorochrome used (e.g. CD4-FITC).

☒ The axis scales are clearly visible. Include numbers along axes only for bottom left plot of group (a 'group' is an analysis of identical markers).

☒ All plots are contour plots with outliers or pseudocolor plots.

☒ A numerical value for number of cells or percentage (with statistics) is provided.

Methodology

Sample preparation

Blood: blood collected in EDTA tubes - RBC lysis step
Synovium: was harvested from ankle and knee after bone marrow flushing from hind legs. Single cell suspension was subsequently obtained after enzymatically digesting the synovial tissue with dispase (1 mg/mL) and collagenase VIII (0.75 mg/mL).

Instrument

CytoFLEX V3-B4-R3 (Beckmann Coulter), Miltenyi MACSQuant16 (Miltenyi), BD FACS Aria III (BD Company) and Imagestream X Mark kII (Amnis)

Software

CytExpert (CytoFLEX), MACSQuantify (MACSQuant), BD FACSDiva (FACS Aria) and Amnis Imagestream (Imagestream) for collection. FlowJo(BD company) and IDEAS (Amnis) for analysis.

Cell population abundance

For all experiments, the entire samples was used for flow cytometric analysis, so no sorting was performed. The liposome-positive cell fraction differed between liposome type and time after injection and is shown throughout the manuscript.
For imagestream analysis, a pre-analysis sorting was done on viable CD45+CD11b+ cell fraction in blood and synovium.

Gating strategy

The gating strategy can be retrieved in Supporting Information 1, 2 (CytoFLEX data), 7 (MACSquant data), 9 (BD FACS Aria sorting), 10 (Imagestream analysis) and 13 (Internalization wizard of IDEAS software).
First viable cells were selected by gating: all cells (1) single cells (2) and viable cells (3). The latter excluded the dead cells in CytoFLEX analysis and both the dead cells as well as the dump chanel (CD19, NK1.1 and CD3e markers) in MACSQuant panel.

Subsequently the different types of myeloid cells were gated in both panels (i.e. monocytes, monocyte-derived macrophages (MoMFs), granulocytes) and others (DCs, B-cells, etc.) in CytoFLEX panels as overviewed in Supplementary Information.

☒ Tick this box to confirm that a figure exemplifying the gating strategy is provided in the Supplementary Information.